J Mater Sci (2009) 44:608–619
DOI 10.1007/s10853-008-3077-0

Microscopy and microanalysis of inorganic polymer cements. 1: remnant fly ash particles

**Redmond R. Lloyd · John L. Provis ·
Jannie S. J. van Deventer**

Received: 9 July 2008 / Accepted: 21 October 2008 / Published online: 10 November 2008

Abstract Accurate and precise electron microscopic analysis of the remnant solid precursor (fly ash and blast furnace slag) particles embedded in an inorganic polymer cement (or "fly ash geopolymer") provides critical information regarding the process of gel binder formation. Differential solubility of phases in the fly ash is seen to be important, with insoluble mullite crystals becoming exposed by the retreat of the surrounding glassy phases. High-iron particles appear to remain largely unreacted, and the use of sectioned and polished specimens provides a view of the inside of these particles, which can show a wide variety of phase separation morphologies and degrees of intermixing of high iron and other phases. Calcium appears to be active in the process of alkali activation of ash/slag blends, although the competitive and/or synergistic effects of ash and slag particles during the reaction process remain to be understood in detail.

Introduction

In the drive toward a sustainable world economy, the development of new construction materials for use in place of at least some of the world's Portland cement consumption is of critical importance. Cement production generates 5–8% of the world's anthropogenic CO_2 emissions, a figure which is predicted to increase dramatically in the coming decades as CO_2 savings are found in other sectors, while the cement industry will be constrained by the dual issues of rising demand and inherent limitations on CO_2 efficiency due to the fundamental chemistry of calcium silicate hydrate binders [1]. Inorganic polymer cements (IPC, and including aluminosilicate 'geopolymers') have been proposed as a solution to some of these problems, as they provide the potential for very significant (on the order of 80%) CO_2 savings while offering at least comparable performance in many areas [2]. However, there are many aspects of IPC technology that remain incompletely understood, in particular the details of the chemical mechanism by which the solid fly ash and blast furnace slag precursors are converted by the action of alkalis into a gel binder phase [3, 4]. Studies of the process of formation of the IPC binder have generally focused on the development of atomic-scale structure [5–12], as that is relatively more accessible (although still complex to measure and describe) when compared with microstructural evolution [13]. The key tool that has the potential to provide a detailed understanding of IPC microstructure and its evolution with time is electron microscopy.

To fully understand IPC formation, the nature of the precursor materials must first be better understood. The majority of particles in fly ashes produced by the combustion of bituminous to sub-bituminous coals, which are often attractive in terms of IPC synthesis, consist primarily of alumina and silica [14, 15]. Within these, the most important phases are typically glass, quartz, and mullite [15]. Mullite crystallizes upon cooling of molten alumina–silica droplets that occur as a result of melting of the clay constituents of the coal [15, 16]. Due to rapid quenching, not all of the liquid crystallizes to mullite, and the fraction that does not crystallize contributes the majority of the glass in fly ash. Lee and van Deventer [17] showed that the aluminosilicate glass present in fly ash is the source of reactive material for IPC formation. The nature of the glass

R. R. Lloyd · J. L. Provis (✉) · J. S. J. van Deventer
Department of Chemical & Biomolecular Engineering,
University of Melbourne, Victoria 3010, Australia
e-mail: jprovis@unimelb.edu.au

in fly ash and its consequences for IPC formation have recently been examined, and found to be more complex than had previously been assumed [18, 19]. Development of an understanding of coal ash glass chemistry and its effect on IPC formation is ongoing, and is central to commercial utilization of IPC.

A common assumption in the field is that metakaolin-based geopolymers provide a satisfactory model for fly ash-based IPC [20]. Through a combination of experimental techniques, in particular NMR, significant progress has been made toward understanding the chemistry of metakaolin-derived geopolymers [21–23]. The current state of knowledge is better at the atomic level than at the microstructural level. There have also been studies conducted using environmental scanning electron microscopy (ESEM) [24, 25], although the interpretation of some of these data is still the subject of some discussion [4]. While there are undeniable similarities between the two systems, it has been demonstrated that such assumptions cannot provide a fully satisfactory explanation of the reactivity of fly ash and the properties of fly ash-based IPC [4, 19]. Fly ash is a highly heterogeneous material [16], and it appears that this significantly affects the quantity and composition of phases available for alkali activation [18].

The situation is further complicated by the incorporation of blast-furnace slag (GGBS) into IPC; this has been shown to improve some properties of both metakaolin-based geopolymers [26] and waste-based IPC [27]. Fundamental understanding of the role of calcium in IPC, in particular when it is derived from GGBS, remains elusive. Furthermore, the interpretation of some early results [28] has led to debate regarding the effect and consequences of GGBS incorporation.

Microstructure is of particular importance for durability; in fact, it defines all aspects of durability. For example, it has been proposed that the acid resistance of IPC is a direct result of the formation of a three-dimensional aluminosilicate framework rather than the calcium silicate hydrate (C–S–H) phases found in Portland and activated slag cements [29]. Therefore whether C–S-H forms [28, 30] or not [31], and if so, how it is distributed, appears central to any understanding of acid resistance of IPC containing GGBS. Similarly, the distribution of pore sizes within concrete is known to control mass transfer [32]; mass transfer is central to almost all aspects of durability including acid resistance, corrosion of reinforcement, sulfate attack, and carbonation.

Given the importance of microstructure to the rational understanding of IPC durability, and the lack of clarity that persists, the aim of this article and its companion [33] is to contribute significantly to the understanding of the microstructure of waste-based IPC. In most IPC three phases are present, intimately mixed: two solid phases, which are the unreacted raw material and the reaction product, and one solution phase. Separation and isolation of these phases has provided a challenge, although some progress has been made [34], but without the ability to separate the phases accurate analysis is difficult. Electron microscopy provides the most accessible means of achieving this, and forms the basis of these articles. This first article will provide the first detailed analysis of the unreacted remnant fly ash and slag particles embedded in the IPC binder, along with some discussion of optimization of electron microscopy data for IPC systems. The second article will then apply the techniques presented here to the detailed investigation of the IPC gel binder structure.

Experimental methods

Materials

The IPC samples studied here were synthesized using fly ash (ASTM Class F) from Gladstone Power Station, Queensland, Australia (supplied by Pozzolanic Industries, Australia) and GGBS supplied by Independent Cement and Lime, Melbourne, Australia. The oxide compositions of these materials are given in Table 1, and their X-ray diffractograms in Fig. 1. The fly ash used contains ~14% mullite, ~7% maghemite, and ~3% quartz; the GGBS is X-ray amorphous [4]. Detailed characterization of this ash, with reference to both the glassy and crystalline phases present, has recently been conducted [18]. The ash particles are comprised of multiple intimately intermixed glassy phases, with crystallites either embedded in the glass or (occasionally) present as discrete particles. Separation into

Table 1 Oxide compositions of raw materials, in wt.%, from X-ray fluorescence analysis

	Fly ash	GGBS
Na_2O	0.28	0.26
MgO	1.35	6.02
Al_2O_3	27.84	13.18
SiO_2	45.46	32.88
P_2O_5	0.53	0.00
SO_3	0.21	3.50
K_2O	0.47	0.32
CaO	5.60	40.05
TiO_2	1.36	0.66
V_2O_5	0.00	0.03
MnO	0.19	0.40
Fe_2O_3	11.21	0.32
LOI	2.71	1.19

LOI loss on ignition at 1000 °C

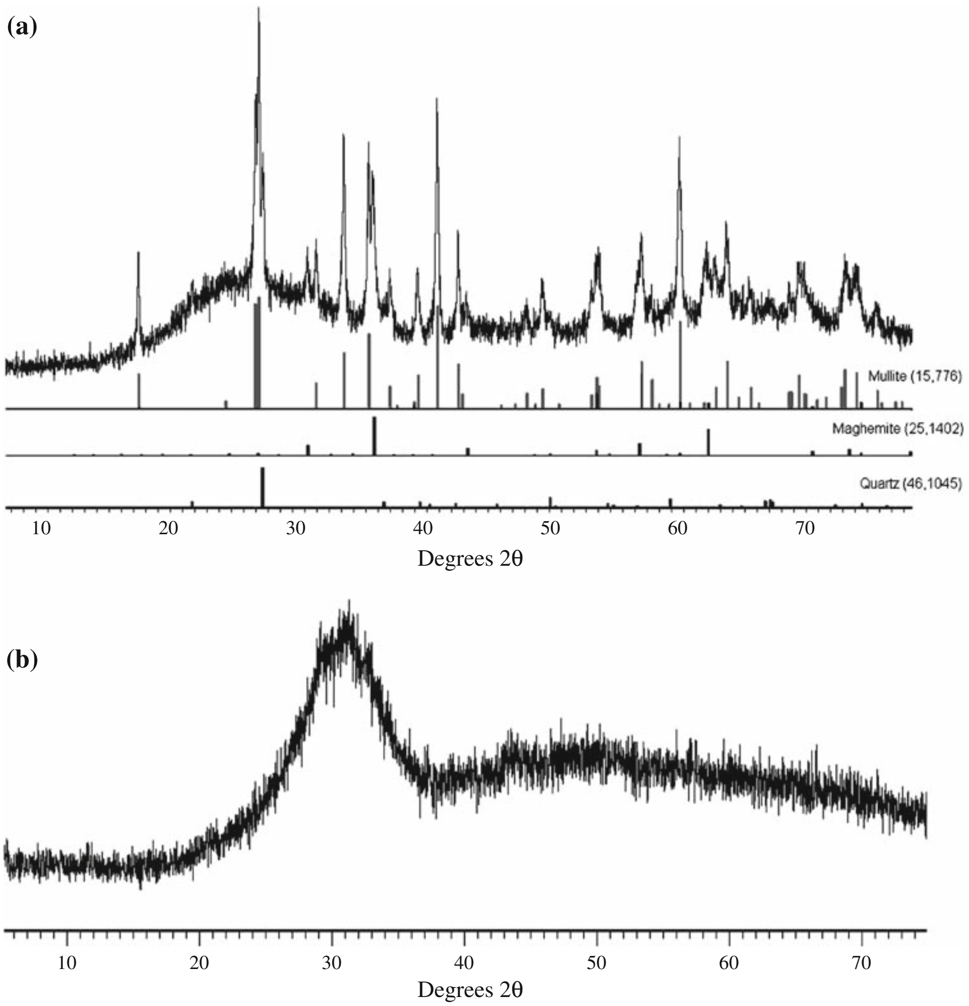

Fig. 1 Cu-K$_\alpha$ diffractograms of the solid aluminosilicate source materials used in this article. **a** Gladstone fly ash. **b** Ground granulated blast-furnace slag

iron-rich and iron-poor phases is observed, and multiple different aluminosilicate glasses with differing Si/Al ratios form due to the effects of metastable immiscibility [18].

The activating solutions used consisted of a blend of commercial sodium silicate solution (Grade N, PQ Australia) with sodium hydroxide solution (50 wt.%, Aldrich, Australia) and RO-grade deionized water, and were formulated so as to provide 7 wt.% SiO_2 and 7 wt.% Na_2O by mass of solid precursor (GFA or GFA + GGBS), and water/binder ratios of 0.325 for fly ash-based samples and 0.350 for ash/slag blends.

For mixed ash-GGBS IPC samples, ash and slag were homogenized in a vibratory mill (laboratory pulverizer) with the milling media removed prior to the addition of the activating solution. This was found to break down agglomerates in the GGBS and provide an even distribution of particles without modification of particle size distribution or particle surfaces. Samples were mixed by hand to homogeneity, and cured in sealed molds at 65 °C for 48 h and then held at 23 °C for a minimum of 28 days before analysis. Care was taken to avoid exposure of prepared samples to the atmosphere to minimize atmospheric carbonation. X-ray diffractometry was conducted using Cu-K$_\alpha$ radiation (Phillips PW1800, operating at 40 kV and 30 mA).

Scanning electron microscopy (SEM)

A Philips XL30F SEM fitted with a cold tungsten field emission source was used for high-resolution imaging. This microscope was typically operated at an accelerating voltage of 5 kV. Samples were coated with a thin layer of conductive carbon for microanalysis and imaging. An FEI Nova NanoLab 200 dual column instrument was used for high-resolution SEM imaging and microanalysis. The electron column had a thermal field emission source and was usually operated at accelerating voltages between 2 and 5 kV. The microscope had secondary electron (SE) and back-scattered electron (BSE) detectors and offered an optional higher-resolution "immersion" mode, in which the electrons are detected within the pole piece, significantly reducing the effects of stray fields on the signal. An

EDAX Genesis X-ray spectrometer was used for microanalysis and elemental mapping.

Sample preparation is very important for accurate SEM analysis of IPC. In particular, it is important to avoid inducing artifacts during polishing and to avoid changes in chemistry prior to microanalysis. The procedure adopted involved sectioning, grinding, and polishing. Polished sections are preferred over fracture surfaces for analysis of IPC as they provide a more representative view of the binder structure, as well as information regarding structures within fly ash particles and the surface smoothness required for accurate microanalysis [4].

After identifying the region of interest, a Leco VC-50 sectioning wheel with a diamond blade was used to section the sample. Sectioning was carried out dry with a wheel speed of 200 rpm. Grinding was carried out using successively finer grades of SiC abrasive bonded to self-adhesive disks on a Leco lapping wheel. Ethanol was used as lubricant. Final polishing was carried out using the same lapping wheel with polishing cloths and successively finer grades of diamond abrasive (ProSciTech, Australia) suspended in lapping oil sold as “Diamond Extender” (Leco, USA). Details of the grinding and polishing procedure followed are presented in Table 2. Epoxy impregnation has been strongly recommended for accurate microscopy of hydrated Portland cements [35]; such treatment was found not to be necessary for many of the specimens studied here, although it is important in the study of IPC specimens that have been degraded by, for instance, acid attack, or those that display low mechanical strength [4].

The FEI Nova NanoLab 200 dual column instrument was also used for preparation of membranes for analysis by transmission electron microscopy (TEM), by focused ion beam (FIB) milling. The ion column had a liquid gallium ion source, and was operated at an accelerating voltage of 30 kV. An EDAX Genesis X-ray spectrometer was used for microanalysis and elemental mapping. Transmission electron microscopy (TEM) was conducted using a JEOL 2010 TEM fitted with a LaB_6 electron source, operated at 200 kV accelerating voltage, and a LINK energy dispersive X-ray spectrometer. Samples were prepared by the ‘lift-out’ technique as described in detail by Lloyd [4].

Table 2 Grinding and polishing steps used for SEM specimen preparation

Step	Disk type	Abrasive	Duration (s)
400 grit	400 grit	SiC	60
800 grit	800 grit	SiC	60
1200 grit	1200 grit	SiC	60
6 μm	Nylon cloth	Diamond	180
1 μm	Short napped cloth	Diamond	300
0.25 μm	Short napped cloth	Diamond	180

Results and discussion

Accurate microanalysis of IPC

A significant complication in X-ray microanalysis is the discrepancy between the effective (observable) beam–specimen interaction volumes for secondary electron generation and characteristic X-ray generation [36]. The secondary electron signal is the primary imaging mode in SEM, while the X-ray signal is used in elemental microanalysis. Although both secondary electrons and X-rays are actually generated in the same interaction volume, secondary electrons have low energy, mostly <10 eV, and are only able to escape from within 2 nm of the surface of the specimen [37]. Conversely, X-rays pass through the sample, albeit with some absorption, and thus the X-ray signal detected includes X-rays generated from within the majority of the interaction volume [36, 37]. The result is that the spatial resolution of the X-ray signal is lower than that of the secondary electron signal. This is widely overlooked in SEM microanalysis of cements, and can mean that the X-rays being detected for microanalysis are from a region not visible in the secondary electron image. This is of critical importance for IPC, which is heterogeneous on the length scale (1–5 μm) of the X-ray interaction volume.

It has previously been assumed that the interaction volume for X-ray microanalysis in cements under typical SEM imaging conditions (20 kV accelerating voltage) extends approximately 1 μm below the specimen surface [38]. To test this for the case of IPC, Monte Carlo simulations of electron trajectories were performed using the computer program CASINO v. 2.42 [39]. Simulations were performed using a bi-layer specimen. On the sample surface was a 25-nm-thick layer of carbon, as was used to provide a conductive coating on the actual physical specimens studied here. Stoichiometry of $NaAlSi_2O_6$ was used for the substrate, with a density of 1580 kg/m^3 as determined for the solid IPC paste. The $\phi\rho Z$ correction was used to account for X-ray absorption and fluorescence within the sample.

Figure 2 shows simulated electron trajectories for 200 electrons at incident electron energies of 20 and 5 keV. At 20 keV, some electrons penetrate more than 5 μm into the sample, meaning that X-rays will be generated from up to this depth below the sample surface; clearly the resolution of microanalysis is worse than has been anticipated for IPC samples. Fortunately, resolution can be improved dramatically by decreasing the accelerating voltage, as shown in Fig. 2b where a 5 keV incident beam gives an order of magnitude improvement in spatial resolution compared to 20 keV.

Quantitative estimation of the resolution that could be expected for SEM microanalysis of IPC at various accelerating voltages, derived from the output of the CASINO simulations, is provided for sodium and silicon in Fig. 3.

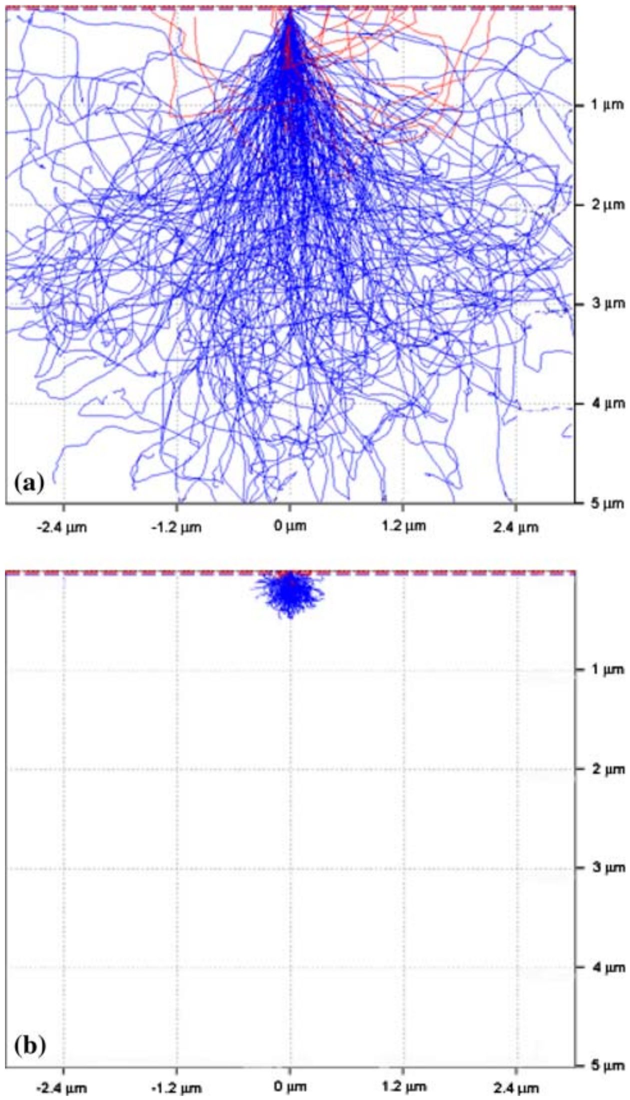

Fig. 2 Simulated electron trajectories for **a** 20 keV and **b** 5 keV primary beam energies, plotted on the same scale. $NaAlSi_2O_6$ substrate with 25 nm layer of C. Simulations conducted using CASINO v.2.42 [39], with 200 electrons simulated per sample

Results for aluminum were very similar to silicon. These plots show the depth at which the "*n*th" percentile of X-rays reaching the X-ray detector is generated. Thus, at 20 keV incident electron energy, 50% of detected sodium X-rays would have been generated from deeper than 1 µm in the sample, 25% from deeper than 2 µm and 5% from deeper than 3.25 µm. Due to the large number of counts necessary for accurate quantitative analysis, the latter figure is probably a good representation of the resolution; for shorter count times and thus fewer detected electrons, for instance when generating compositional maps, the useful resolution is probably between 2 and 3 µm. At 5 keV, resolution is significantly improved; quantitative analyses could be performed with resolution of approximately 300 nm.

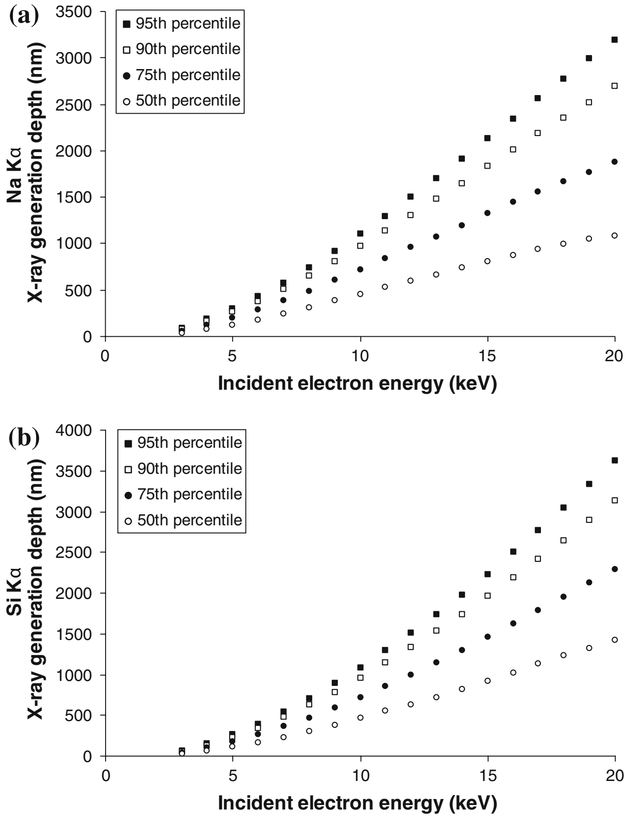

Fig. 3 Depth of X-ray generation versus incident electron energy for **a** Na-K_α X-rays and **b** Si-K_α X-rays, after application of absorption and fluorescence corrections. "*n*th percentile" indicates the proportion of X-rays generated at that depth or shallower. 10^6 electron trajectories were simulated for each incident electron energy. Simulations conducted using CASINO v.2.42 [39]

It should be noted that the X-ray production efficiency (ionization cross section) varies strongly with overvoltage, *U*, defined as the ratio of incident electron energy to critical ionization energy, E/E_{crit} [40]. The ionization cross section is maximized at an overvoltage of approximately 5 [41], although 2 is usually considered sufficient for microanalysis. Using 5 keV will result in low X-ray production efficiency for K and Ca-K_α X-rays (which have E_{crit} of 3.607 and 4.038 keV, respectively) and, obviously, no K_α X-rays for elements with E_{crit} higher than 5 keV (i.e., vanadium and above). However, for heavier elements of interest such as Fe, the L-series X-rays may be used for analysis when the incident electron energy is low.

Based on Fig. 3, and despite the disadvantage of low X-ray production efficiency, it is recommended that microanalysis of IPC be conducted at accelerating voltages lower than are commonly used, e.g., 5 kV instead of 20 kV. Figure 3 may be useful in selecting an appropriate accelerating voltage for the size of the features being examined; the accelerating voltage used should be reconciled with the ionization energies of the elements of interest.

Aluminosilicate particles

Examination of particle remnants in cured IPC provides key insight into some of the processes occurring during reaction. Figure 4a shows a typical polished section of fly ash IPC paste. Numerous circular cavities are evident in the gel; the presence of crystals within them indicates that they are the insoluble remnants left behind by dissolution of the surrounding glass. This is demonstrated by the main particle in Fig. 4a and magnified sections in Fig. 4b and c. The center of the particle appears to be homogeneous and contains levels of aluminum and silicon typical of fly ash. Surrounding the particle is a network of tabular, apparently crystalline particles and outside that, the reaction gel. The homogeneous gel outside the perimeter of the crystalline region must have solidified before the crystals were exposed, or it would have penetrated and filled the voids between crystals. The crystals are therefore remnants left behind by the retreat of the glass surface as it dissolved. Confirmation is provided by microanalysis, which indicates an Al:Si ratio well in excess of unity. In the system studied this can only occur in mullite or other high temperature phases; see Aramaki and Roy [42], for instance, for a phase diagram. As mullite only forms at high temperature and in

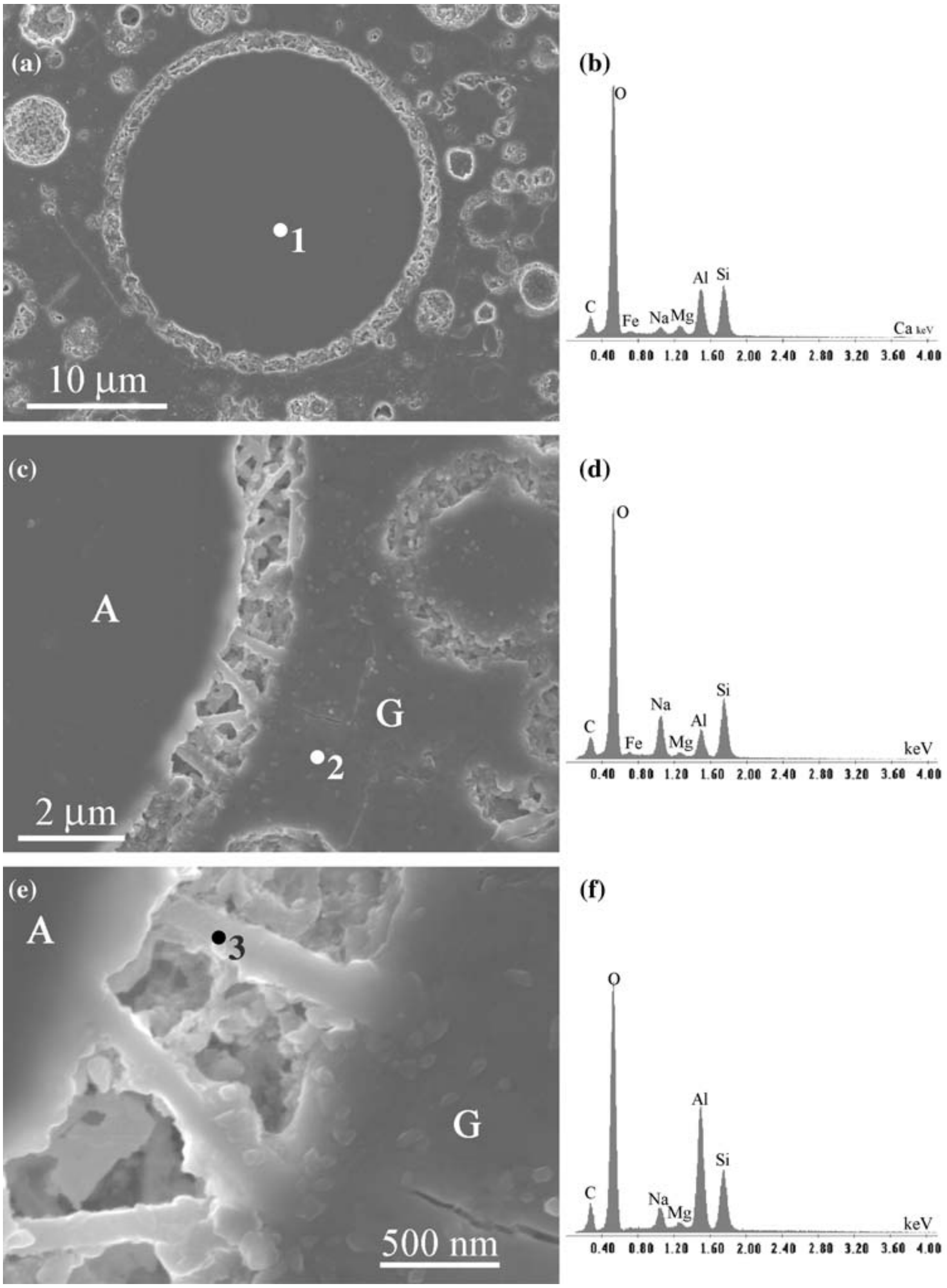

Fig. 4 **a** Secondary electron image of a polished section of fly ash-based IPC paste. Panels **c** and **e** are magnified portions of (**a**); ‘A’ and ‘G’ indicate the ash particle and gel, respectively. Points indicated in the electron images correspond to the X-ray spectra: **b** is taken at point 1, **d** at point 2, and **f** at point 3

the absence of alkali or alkaline earth cations, it cannot be a surface precipitate.

The small amount of sodium indicated in Fig. 4c is very unlikely to be a constituent of the mullite, and is probably a result of beam spreading and inclusion of some of the surrounding material in the X-ray generation volume.

The identity of these crystals is supported by TEM, as shown in Fig. 5. It is apparent that mullite in fly ash can have two different habits: needle-like crystals as in Fig. 5a or smaller, more rounded crystals as in Fig. 5b. The electron diffraction patterns confirm that both types are crystalline. The rounded crystals are often seen in cavities in polished sections, as shown in Fig. 5e and f, exposed by the dissolution of surrounding glass.

Particles such as those shown in Figs. 4 and 5 demonstrate phase separation in aluminosilicate fly ash particles. During coal combustion, the non-volatile inorganic components melt and form liquid droplets. Mullite crystallizes from these, leaving behind an aluminum-depleted liquid, which solidifies to a glass on cooling; thus, both glass and mullite exist within the same particle. Microscopic examination of reacted particles shows the difference in solubility between mullite and glass and confirms that mullite plays little or no part in IPC gel formation. It is clear that crystals visible on the surface of particles may originate from within the particles themselves, left behind by the dissolution of more soluble glass, rather than result from crystallization during reaction.

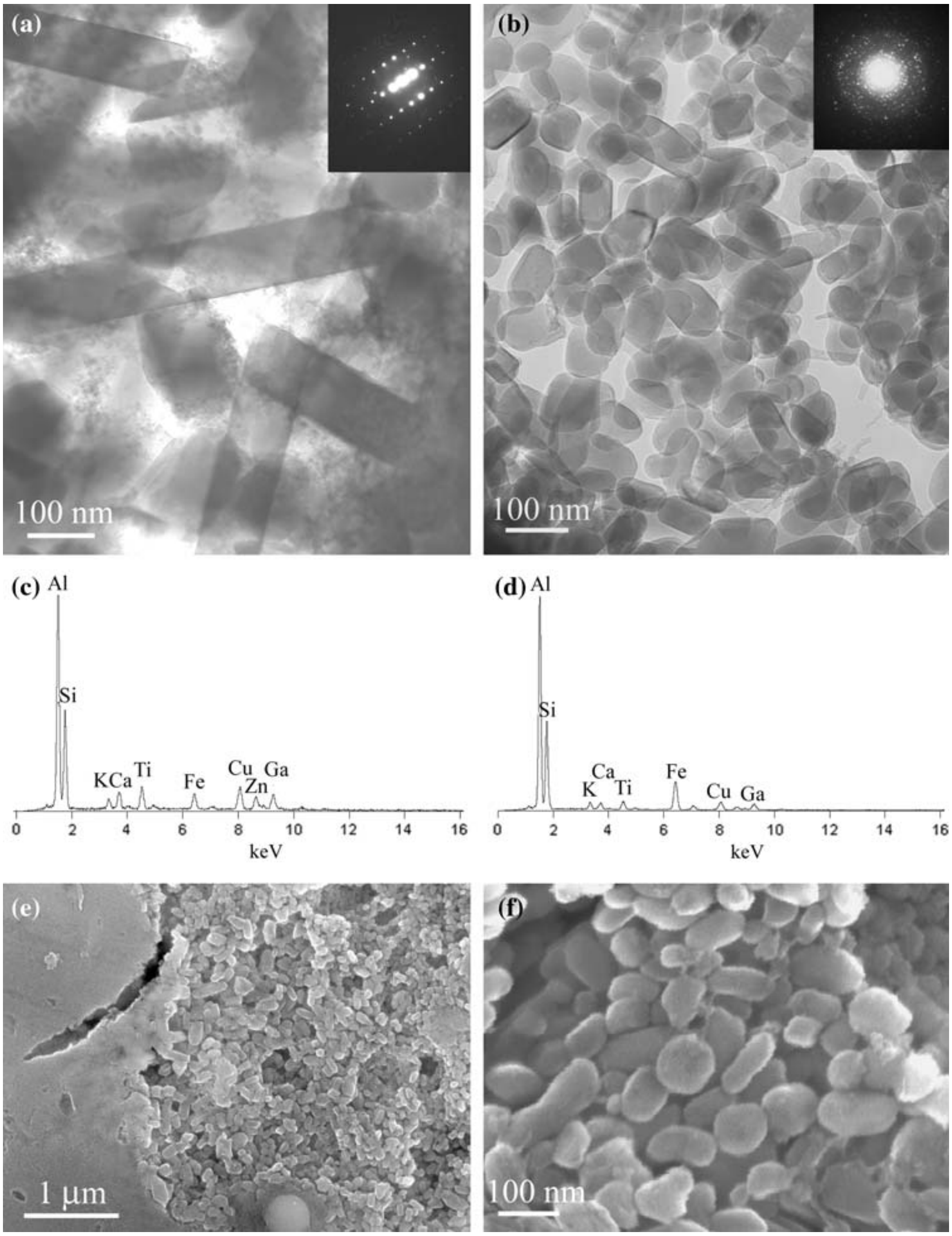

Fig. 5 Different habits of mullite in fly ash remnants, revealed after dissolution of the surrounding glass during IPC formation. **a**, **b** TEM bright-field images of mullite crystals. The selected-area electron diffraction patterns (inset) and X-ray spectra shown in (**c**) and (**d**) confirm the identification. Cu, Ga, and Zn are artifacts in the spectra. **e**, **f** SEM secondary electron images of polished sections of IPC. Mullite, similar to that shown in (**b**), has been exposed by dissolution of the surrounding silica-rich glass

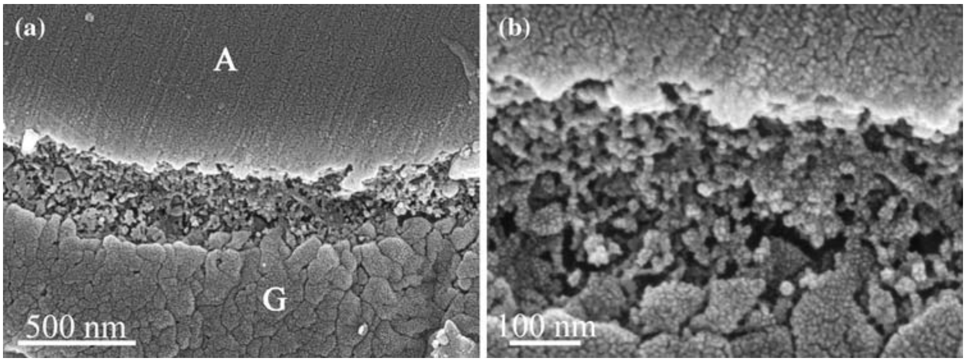

Fig. 6 Secondary electron images of a polished section of fly ash-based IPC paste, aged for 2 years at 23 °C. **a** The interface between ash particle ‘A’ and reaction gel ‘G’ is clearly different to the interfaces involving particles containing crystalline mullite as shown in Fig. 5. **b** The interface shown in (**a**), at higher magnification. A less soluble phase appears to have been exposed by the retreat of dissolving glass

It has been shown that the aluminosilicate glass present in the fly ashes studied here can also undergo phase separation without crystallization to mullite [16, 18]. The result is two glassy phases, one silica-rich and the other rich in alumina, interspersed in regions of size 50 nm or less. Should there be a difference in solubility between the two phases, this may be visible in polished sections of the reacted particles in the same way as has already been demonstrated for crystalline mullite and glass. Images of very fine scale inhomogeneity were obtained from fly ash-based IPC pastes aged at 23 °C for 2 years, shown in Fig. 6. This phase is interconnected and extremely fine; the morphology is consistent with metastable immiscibility in aluminosilicate glasses [43]. These images may imply differential solubility of the aluminosilicate glass phases present in fly ash, as discussed by Keyte [18]. In the absence of supporting information from microanalysis or TEM, however, it is not possible to confirm the identity of this material.

Iron-containing particles

Iron makes up a significant portion of many coal fly ashes, and crystalline iron-containing phases (particularly maghemite) are apparent in the X-ray diffraction data in Fig. 1. Iron in fly ash is also found as a substituent in mullite [44] and in iron silicate phases, which may be crystalline or amorphous [45].

There is significant interest in the fate of iron in fly ash during IPC formation. Fernández-Jiménez et al. [46] proposed a link between arsenic and iron in IPC used for waste immobilization. Xu et al. [47] suggested that during alkaline activation iron dissolves from iron-rich fly ash particles and forms either crystalline hydrates on the surface of the particles or colloidal hydrates, depending on the activating conditions. The formation of crystalline hydrates was linked to hindered strength development, while the colloidal hydrates were associated with better strength development. However, other studies using fly ashes with magnetic iron-containing particles being removed have shown little effect on strength development in the presence or absence of iron [19].

Due to the high atomic number of iron relative to most other IPC constituents, iron-rich phases appear bright in BSE images. Some typical iron-rich particles are shown in Fig. 7, and are similar to those reported in the literature [48]. Phase separation is clearly visible in BSE images, and was confirmed by microanalysis. The iron content of fly ash particles varies: the particle in Fig. 7a contains almost pure iron oxide, while those in Fig. 7b, f, and g contain a mixture of iron-rich and silica-rich phases. Substitution of magnesium and aluminum into the iron-rich spinel phase, as shown in Fig. 7d, is in good agreement with the literature [49, 50].

Particles rich in iron are largely inert during alkali activation, which is apparent from the intact nature of the spheres observed in the reacted paste. Some particles, however, demonstrate the difference in solubility between the iron-rich and silica-rich phases. These particles show deep etching of the silica-rich phase, leaving the iron-rich phase intact, as shown in Fig. 8. This enables clarification of the observations of Xu et al. [47]: the proposed crystalline iron hydrates identified on the surface of ash particles by those authors are actually the insoluble iron-rich phase left behind as the silica-rich phase dissolves, rather than being due to reprecipitation of dissolved iron species. Based on the highly selective dissolution behavior observed, it appears that only iron present in the silica-rich phase is available to dissolve. Microanalysis of the silica-rich phase, e.g., Fig. 7e, indicates that some iron is present; due to the fine scale of the phase separation, however, beam spreading would be expected to cause some of the iron-rich phase to be included in the analyzed volume. Therefore, it is not possible to quantify the amount of iron

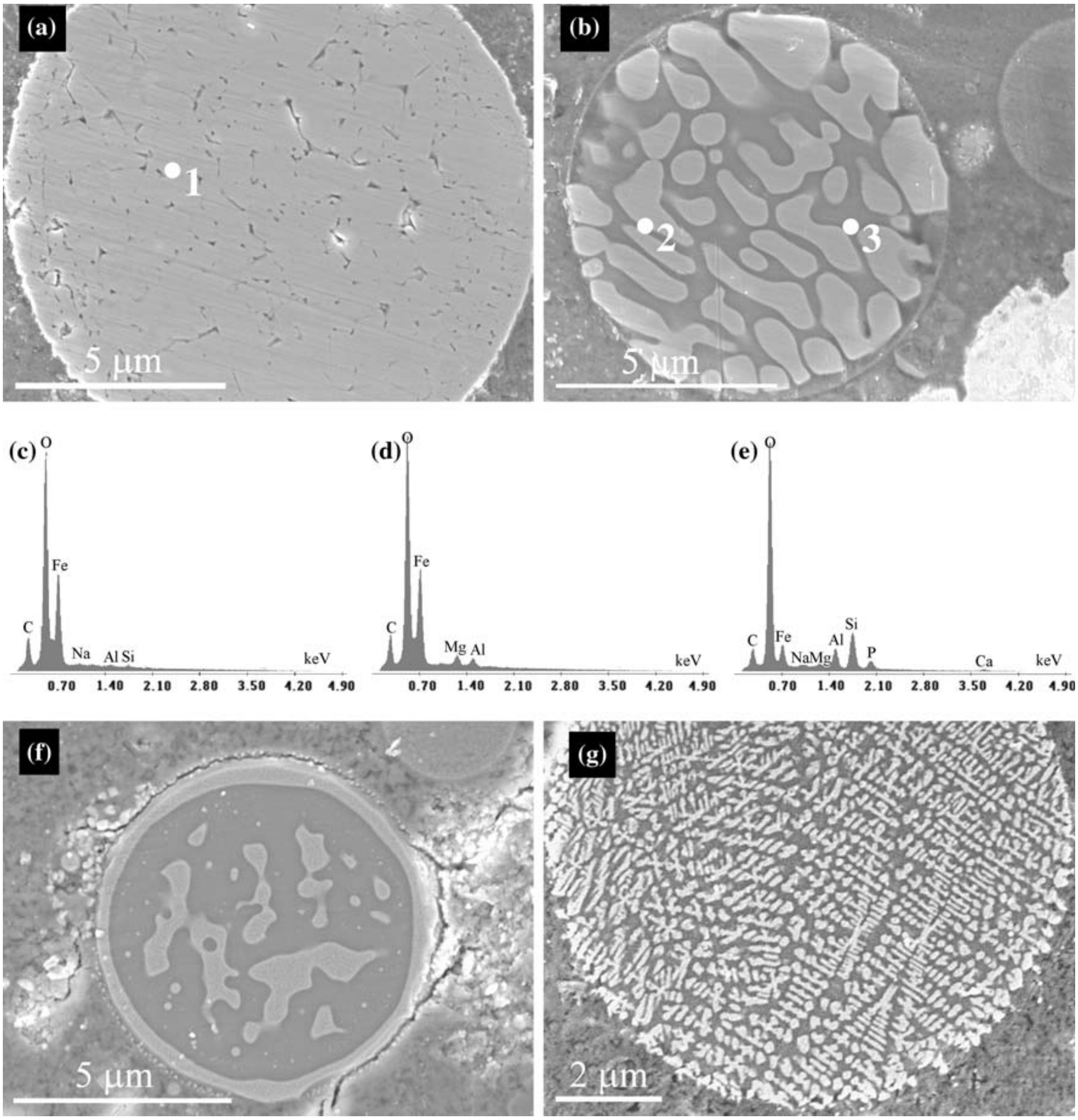

Fig. 7 BSE images of iron-containing particles in polished sections of cured IPC. **a** Sphere containing mostly iron with traces of silica in the interstices. **b** Typical particle demonstrating phase separation into iron-rich (*lighter*) and iron-deficient (*darker*) regions. **c** X-ray spectrum of point 1 in (**a**), showing almost pure iron oxide. **d**, **e** X-ray spectra of iron-rich (point 2) and silica-rich (point 3) phases in (**b**). **f** Unusual particle morphology, with an iron-rich rim and phase separated internal structure. **g** Dendritic iron-rich particle, showing fine-grained phase separation

present by SEM/EDX, or even to say conclusively whether there is any in the silica-rich phase.

Using various experimental techniques, in particular Mössbauer spectroscopy and electron paramagnetic resonance spectroscopy, other authors have been able to examine the deportment of iron in fly ash. Bayukov et al. [49] showed that the magnetic fraction of fly ash contained predominantly Mg-, Al-, and Ti-substituted magnetite, along with divalent iron in a silicate phase. Hinckley et al. [51] noted iron in numerous phases including hematite, magnetite, mullite, goethite, and in silicates. Of particular relevance to the study of IPC is the work of Warren and Dudas [50], who performed a very detailed investigation of the partitioning of elements in the magnetic fraction of fly ash. They found that magnetic fly ash particles contained three phases: a reactive outer coating of aluminosilicate glass rich in Fe, Ca, Na, K, and Mg, a crystalline magnetite, and an interstitial aluminosilicate glass. Not more than 5% of the iron in these particles was soluble. Vereshchagina et al. [52] examined the cenospheres in fly ash and found that at low iron concentration, 3–4 wt.% as Fe_2O_3, iron was distributed both as ions and in 3–5 nm spinel domains

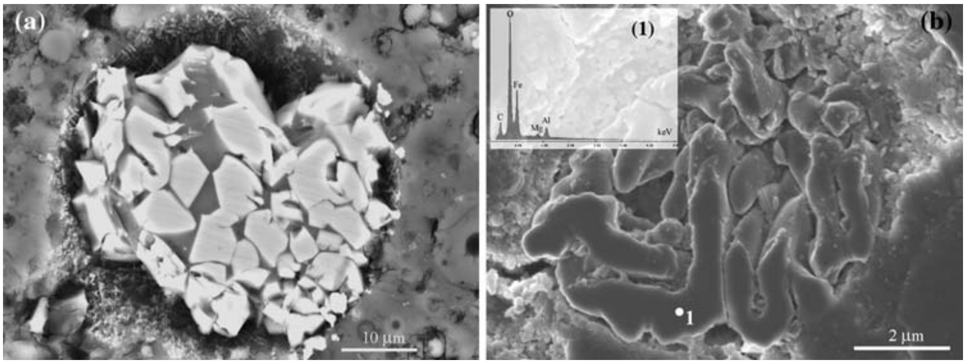

Fig. 8 **a** BSE image of an iron-rich sphere showing the outline of the original surface of the particle and partial dissolution of the silica-rich phase. **b** Secondary electron image of the remnant of an iron-rich sphere showing complete dissolution of the silica-rich phase. The iron-rich phase is left intact. The X-ray spectrum, inset, collected from the point marked, shows Mg- and Al-substituted iron oxide

dispersed in the aluminosilicate glass. At higher iron content, greater than about 7 wt.% Fe_2O_3, magnetite began to form as well.

Thus, it is clear that only a small quantity of the iron in fly ash is in a form that could participate in IPC formation. Of this, not all will dissolve, as demonstrated by the relative lack of iron-rich particles in which dissolution of the interstitial glassy phase is apparent. This may be due to compositional variation in the glass, resulting in different solubility, or simply a result of occlusion of the glass by the inert iron phase.

The fate of soluble iron is not yet clear—when it dissolves it may disperse evenly through the gel or be concentrated near the particle from which it dissolved. X-ray analyses in the SEM almost always indicate the presence of some iron, even far from the surface of iron-rich particles, so the former may be the case. Whether Fe^{3+} substitutes for Al^{3+} in the aluminosilicate gel is not certain; results presented by Perera et al. [53] indicate that it does not; however, this remains inconclusive due to experimental difficulties they encountered. It is now clear, however, that iron does not form large hydrates on the surface of iron-rich particles, as proposed by Xu et al. [47]. A similar mechanism whereby dissolved iron species were predicted to precipitate, as hydroxides or oxyhydroxides, has also been suggested [3, 20]. However, in the light of the new findings presented here, this suggestion must be re-evaluated, with the additional consideration that dissolved silica is known to inhibit precipitation of iron hydroxides [54]. Clearly, much work remains to clarify the fate of iron dissolved from fly ash under the conditions of IPC formation.

Calcium-containing particles

Where GGBS is added to fly ash-based IPC formulations, the undissolved remnants of calcium-rich particles are also easy to locate using BSE imaging, as GGBS has a distinctive angular particle shape and relatively high mean atomic number compared to other particles present due to its higher calcium content.

In BSE images of blended pastes, the calcium-containing grains are surrounded by dark rims as shown in Fig. 9a. X-ray microanalysis shows that these rims are depleted in calcium and aluminum, contain similar levels of magnesium and silicon to bulk GGBS grains, and are enriched in sodium. This issue will be explored in further detail in Part 2 of this series of articles [33]. The presence of reaction rims is an indication that dissolution of calcium from GGBS continues after the paste has set. It appears that magnesium does not disperse into the gel to the same extent as calcium. It is unclear whether the magnesium-containing phase is a hydrate, i.e., a reaction product, or a residual insoluble glass phase. Arguments for both exist: Wang and Scrivener [55] and Brough and Atkinson [56] identified hydrotalcite ($Mg_6Al_2CO_3(OH)_{16}\cdot 4H_2O$) by XRD and by inference from X-ray microanalyses of alkali-activated slag pastes. This implies dissolution of magnesium and subsequent precipitation of magnesium compounds. XRD failed to show hydrotalcite for the samples studied in this work; however, they were not exposed to CO_2 so the absence of this phase is inconclusive. Phase separation in the CaO–MgO–Al_2O_3–SiO_2 system is known, however [57], and separation of the glass into phases of differing solubilities could also occur [58]. Thus, the presence of magnesium in grain remnants could result from a sparingly soluble magnesium-containing phase, rather than the formation of a magnesium-rich hydrate. Although it is not certain which process occurs, it is known that while magnesium is able to participate in formation of hydrated silicate gels, the preference for this is much less strong than in the case of calcium [59].

High-resolution images of GGBS grain remnants are shown in Fig. 9b–d. Different morphologies were observed

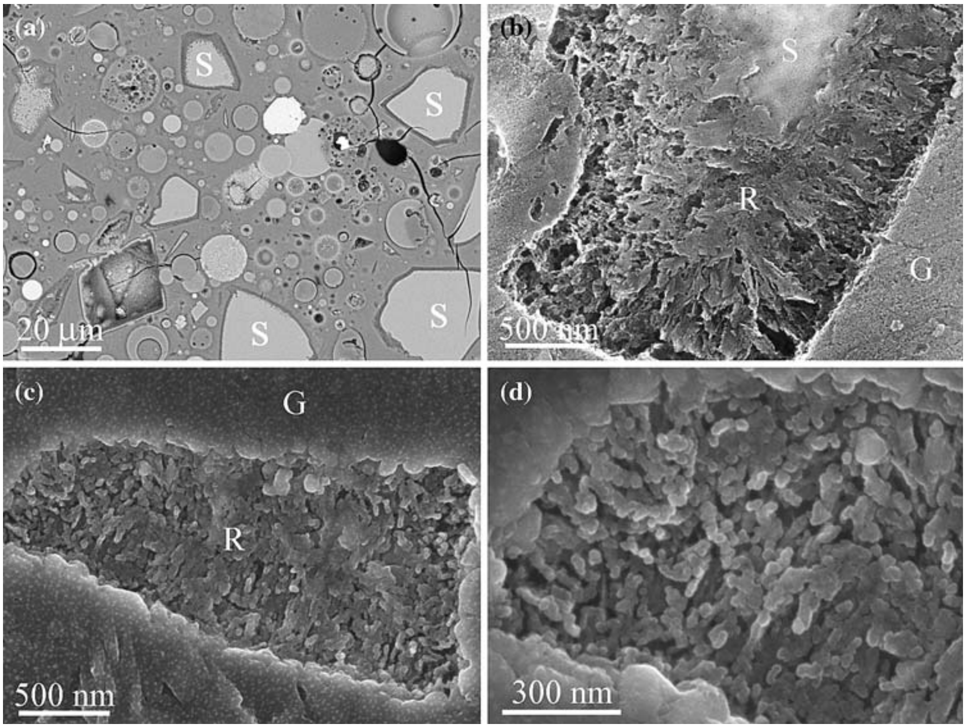

Fig. 9 Images of polished sections of blended GFA:GGBS pastes. **a** 25% GGBS paste with some of the slag grains identified with an 'S' (BSE). The grains have dark rims depleted in Ca but rich in Mg. **b** Remnant of a partially dissolved slag grain in 50% GGBS paste. 'S' is the undissolved portion of the slag grain, 'G' is the gel, and 'R' is the product within the reaction rim (SE). **c** Remnant of a different slag grain in 50% GGBS paste, showing almost complete slag dissolution and very different morphology (SE). **d** Magnified portion of (**c**). Microanalysis indicates Si:Al:Ca ratios of ~3:1:1; however, due to beam spreading these values must be considered indicative at best

for samples produced from different batches of slag and activated under different conditions. The remnants in Fig. 9b display 'crumpled foil' morphology similar to many calcium silicate hydrates. The remnants in Fig. 9c and d displayed very different structures, and contained Si, Al, and Ca but very little or no Mg. This is quite contrary to the observation of reaction rims in Fig. 9a. Clearly, the chemistry of the slag and the activating solution has a significant effect on the nature and distribution of the reaction products formed. It may also be that there are interactions between the components released by the dissolving ash and slag particles which influence each other; it is becoming increasingly clear that the products formed in a mixed ash–slag system are not simply a combination of the phases that would be observed if each of these materials were alkali activated in isolation. Whether these effects are synergistic or competitive also remains to be seen; however, a combination of the two is considered to be the most probable scenario based on the evidence available. A detailed investigation of the effect of slag composition and activating conditions on the microstructure of blended IPC is beyond the scope of this work, but would undoubtedly be of benefit to the field.

Conclusions

Study of the remnant fly ash and slag particles left embedded in a hardened IPC binder can provide very significant information regarding the process of formation of the IPC binder. The remnant particles obviously represent the phases which for various reasons did not dissolve during alkali activation. This means that by analyzing which phases out of those that were originally present are still observable in the hardened binder, a more detailed understanding of the effects of variable ash particle reactivity on IPC formation can be developed. This is believed to be central to the understanding of the mechanism of IPC formation, but relies on accurate microstructural analysis if it is to be understood.

Differential solubility of phases was observed in aluminosilicate, iron-rich, and calcium-containing particles derived from fly ash or blast furnace slag; this has implications for the interpretation of SEM images and challenges previous theories regarding the fate of various components in IPC. Mullite crystals become exposed by the retreat of glassy phases in ash particles during dissolution, meaning that it is important to understand the mullite content of an ash if its reactivity is to be determined. A high iron content appears to render particles relatively unreactive, and phase segregation in iron-containing particles can mean that compositional information obtained even at an individual particle level is not necessarily able to represent its potential for reactivity in IPC formation. Calcium appears to be active in the process of alkali activation of ash/slag blends, although it is not obvious from electron microscopy whether discrete high-calcium binder regions are formed or whether the calcium is incorporated into the main aluminosilicate gel binder. It is clear from the morphology and chemistry of the remnant ash and slag particles in IPC that their dissolution continues after IPC setting. Understanding these issues provides a basis by which the composition and microstructure of the IPC gel binder phase can be rationalized, and is a key aspect of controlling the microstructure and performance of the IPC as a whole.

Acknowledgements Partial financial support for this work was provided by the Australian Research Council (ARC), through Discovery Project grants awarded to J.S.J. van Deventer and through the Particulate Fluids Processing Centre, a Special Research Centre of the ARC.

References

1. Taylor M, Tam C, Gielen D (2006) Energy efficiency and CO_2 emissions from the global cement industry. International Energy Agency, Paris
2. Duxson P, Provis JL, Lukey GC, van Deventer JSJ (2007) Cem Concr Res 37:1590
3. Duxson P, Fernández-Jiménez A, Provis JL, Lukey GC, Palomo A, van Deventer JSJ (2007) J Mater Sci 42:2917. doi:10.1007/s10853-006-0637-z
4. Lloyd RR (2008) Ph.D. thesis, University of Melbourne, Australia
5. Palomo A, Banfill PFG, Fernandéz-Jiménez A, Swift DS (2005) Adv Cem Res 17:143
6. Provis JL, van Deventer JSJ (2007) Chem Eng Sci 62:2309
7. Provis JL, van Deventer JSJ (2007) Chem Eng Sci 62:2318
8. Rees CA, Provis JL, Lukey GC, van Deventer JSJ (2007) Langmuir 23:9076
9. Criado M, Fernández-Jiménez A, de la Torre AG, Aranda MAG, Palomo A (2007) Cem Concr Res 37:671
10. Criado M, Fernández-Jiménez A, Palomo A, Sobrados I, Sanz J (2008) Micropor Mesopor Mater 109:525
11. Rahier H, Wastiels J, Biesemans M, Willem R, van Assche G, van Mele B (2007) J Mater Sci 42:2982. doi:10.1007/s10853-006-0568-8
12. De Silva P, Sagoe-Crentsil K, Sirivivatnanon V (2007) Cem Concr Res 37:512
13. Fernández-Jiménez A, Palomo A, Criado M (2005) Cem Concr Res 35:1204
14. Gieré R, Carleton LE, Lumpkin GR (2003) Am Miner 88:1853
15. Vassileva SV, Menendez R, Alvarez D, Diaz-Somoano M, Martinez-Tarazona MR (2003) Fuel 82:1793
16. Hemmings RT, Berry EE (1988) In: McCarthy GJ, Glasser FP, Roy DM, Hemmings RT (eds) Materials research society symposium proceedings, vol 113. Materials Research Society, Pittsburgh, pp 3–38
17. Lee WKW, van Deventer JSJ (2002) Colloids Surf A 211:49
18. Keyte LM (2008) Ph.D. thesis, University of Melbourne, Australia
19. Keyte LM, Lukey GC, van Deventer JSJ (2005) In: Nizhou A (ed) Proceedings of WasteEng 2005, Albi, France, 2005. CD-ROM proceedings
20. van Deventer JSJ, Provis JL, Duxson P, Lukey GC (2007) J Hazard Mater A139:506
21. Duxson P, Provis JL, Lukey GC, Mallicoat SW, Kriven WM, van Deventer JSJ (2005) Colloids Surf A 269:47
22. Duxson P, Provis JL, Lukey GC, Separovic F, van Deventer JSJ (2005) Langmuir 21:3028
23. Provis JL, Duxson P, Lukey GC, van Deventer JSJ (2005) Chem Mater 17:2976
24. Wei S, Zhang Y-S, Wei L, Liu Z-Y (2004) Cem Concr Res 34:935
25. Zhang Y, Sun W, Jin Z, Yu H, Jia Y (2007) Mater Lett 61:1552
26. Davidovits J, Sawyer JL (1985) US Patent 4,509,985, US Patent Office
27. Li Z, Liu S (2007) J Mater Civil Eng 19:470
28. Yip CK, van Deventer JSJ (2003) J Mater Sci 38:3851. doi:10.1023/A:1025904905176
29. Allahverdi A, Škvára F (2001) Ceram-Silik 45:81
30. Buchwald A, Hilbig H, Kaps C (2007) J Mater Sci 42:3024. doi:10.1007/s10853-006-0525-6
31. Lecomte I, Henrist C, Liégeois M, Maseri F, Rulmont A, Cloots R (2006) J Eur Ceram Soc 26:3789
32. Bejaoui S, Bary B (2007) Cem Concr Res 37:469
33. Lloyd RR, Provis JL, van Deventer JSJ (2008) J Mater Sci, in press (Part 2 of this series). doi:10.1007/s10853-008-3078-z
34. Fernández-Jiménez A, de la Torre AG, Palomo A, Lopez-Olmo G, Alonso MM, Aranda MAG (2006) Fuel 85:1960
35. Kjellsen KO, Monsøy A, Isachsen K, Detwiler RJ (2003) Cem Concr Res 33:611
36. Goodhew P, Humphreys J, Beanland R (2001) Electron microscopy and analysis, 3rd edn. Taylor and Francis, London
37. Egerton RF (2005) Physical principles of electron microscopy. Springer, New York
38. Scrivener KL (2004) Cem Concr Compos 26:935
39. Drouin D, Couture AR, Joly D, Tastet X, Aimez V, Gauvin R (2007) Scanning 29:92
40. Joy DC (1998) J Microsc 191:74
41. Williams DB, Carter CB (1996) Transmission electron microscopy: a text book for materials science. Plenum Press, New York
42. Aramaki S, Roy R (1962) J Am Ceram Soc 45:229
43. MacDowell JF, Beall GH (1969) J Am Ceram Soc 52:17
44. Gomes S, François M (2000) Cem Concr Res 30:175
45. Patil MD, Eaton HC, Tittlebaum ME (1984) Fuel 63:788
46. Fernández-Jiménez A, Lachowski EE, Palomo A, Macphee DE (2004) Cem Concr Compos 26:1001
47. Xu H, Lukey GC, van Deventer JSJ (2004) In: Malhotra VM (ed) Proceedings of 8th CANMET/ACI international conference on fly ash, silica fume, slag and natural pozzolans in concrete. American Concrete Institute, Las Vegas, pp 797–820
48. Kutchko BG, Kim AG (2006) Fuel 85:2537
49. Bayukov OA, Anshits NN, Balaev AD, Sharonova OM, Rabchevskii EV, Petrov MI, Anshits AG (2005) Inorg Mater 41:50
50. Warren CJ, Dudas MJ (1989) Sci Total Environ 84:223
51. Hinckley CC, Smith GV, Twardowska H, Saporoschenko M, Shiley RH, Griffen RA (1980) Fuel 59:161
52. Vereshchagina TA, Anshits NN, Maksimov NG, Vereshchagin SN, Bayukov OA, Anshits AG (2004) Glass Phys Chem 30:247
53. Perera DS, Cashion JD, Blackford MG, Zhang Z, Vance ER (2007) J Eur Ceram Soc 27:2697
54. Swaddle TW (2001) Coord Chem Rev 219–221:665
55. Wang S-D, Scrivener KL (1995) Cem Concr Res 25:561
56. Brough AR, Atkinson A (2002) Cem Concr Res 32:865
57. Fredericci C, Zanotto ED, Ziemath EC (2000) J Non-Cryst Solids 273:64
58. Tsuyuki N, Koizumi K (1999) J Am Ceram Soc 82:2188
59. Brew DRM, Glasser FP (2005) Cem Concr Res 35:85